The International Journal of Advanced Manufacturing Technology (2019) 101:461–474
https://doi.org/10.1007/s00170-018-2925-6

ORIGINAL ARTICLE

Robotic grinding of a blisk with two degrees of freedom contact force control

Fan Chen[1] · Huan Zhao[1] · Dingwei Li[1] · Lin Chen[1] · Chao Tan[1] · Han Ding[1]

Received: 27 July 2018 / Accepted: 23 October 2018 / Published online: 3 November 2018
© Springer-Verlag London Ltd., part of Springer Nature 2018

Abstract
This paper presents a novel two degrees of freedom (DOFs) contact force control method for robotic blisk grinding. The grinding tool is controlled to automatically adapt to the curvity change of the blisk blade and maintain a constant contact force as expected. A smart end effector is used as the actuating device for contact force control. The proposed force controller includes a gravity compensation module, a force prediction module, and a force-position controller. The direction and amplitude of the contact force are predicted with the force prediction module and are controlled with the force-position controller. The tool path of the robotic blisk grinding process is generated and optimized so that the contact points between the tool tip and the workpiece are evenly distributed along the grinding path. Both simulations and experiments are carried out to validate the effectiveness of the proposed method. The results show that the proposed method provides a good contact force control performance, with less than 1 N force fluctuation. The surface finish and roughness are significantly improved compared to the case without force control. The grinding efficiency is raised by about sixfold compared to the case with one DOF force control.

Keywords Robotic grinding · Blisk · Smart end effector · Contact force control

1 Introduction

Blisks are the key parts involved in energy conversion in an aero-engine. The machining accuracy and surface quality of a blisk directly determine its performance, efficiency, and life time [1–3]. The design requirement of the surface roughness of a blisk is normally less than 0.4 μm [4]. Thus, grinding is required after milling of a blisk. Due to the complexity of the blisk surface, the grinding of blisks is largely carried out manually by skilled workers. However, manual grinding is labor intensive and time consuming and produces inconsistent quality [5].

Automated blisk grinding would be invaluable in the industry; the time savings and cost savings would be substantial. This fact has attracted extensive research to investigate possible methods of realizing automated blisk grinding process. Shi et al. [4, 6, 7] and Xiao et al. [8–10] have proposed to use a five-axis computer-numerical control (CNC) machine tool with a constant force control system for automated blisk grinding and turbine blade grinding. But a five-axis CNC machine tool is normally quite expensive. Industrial robots have been proven to be a more economical solution for automation. The robot can be programmed to carry out the grinding jobs and can achieve the required surface quality and machining consistency with active contact force control. The existing active force control methods can be broadly categorized as through-the-arm and active end effector force control [11].

Through-the-arm force control uses force sensors to determine the tool-to-part contact force and adjusts the robot's position accordingly to achieve a constant contact force. Thomessen et al. [12] present a through-the-arm force control strategy for robotic grinding of large hydro turbine blades. A three-axis force sensor is installed between the robot end effector and the grinding tool to sense the contact force, and an external force control loop is added outside the original position control loop of the robot for active contact force control. Park [13] develops a parametric model of the grinding force in the disc-grinding operation, and implements a model reference adaptive pole placement controller for active force control. Minami [14] proposed a sensorless force control method

✉ Huan Zhao
huanzhao@hust.edu.cn

[1] State Key Lab of Digital Manufacturing Equipment and Technology, Huazhong University of Science and Technology, Wuhan, China

for robotic grinding. The grinding force is expressed as a state and is obtained by calculating the dynamic equations of the system. Sun [15] implemented a relative reference calibration method before the robotic grinding process to eliminate the relative error between the tooling system and the workpiece, and applied on-line force compensation during the grinding process to achieve the constant contact force. Different control algorithms are further studied in [16–18] for the through-the-arm force control in the robotic machining applications. In the through-the-arm force control method, it does not employ extra devices for contact force generation. Instead, the robot itself is used to generate the contact force. Therefore, the low positioning accuracy of the robot may limit the achievable force control performance.

Active end effector force control senses the tool-to-part contact force with its embedded force sensor and adjusts the tool compliance through utilization of actuators. Since extra positioning device is implemented for force generation, the contact force control does not couple with the robot's motion control, and it is able to achieve better force control performance. Xi et al. [11, 19] propose an active end effector for contact force control in robotic grinding. The presented end effector has a pneumatic spindle that can be extended and retracted by three pneumatic actuators to provide tool compliance. ATI Industrial Automation has developed an active force controlled axial-compliant tool which is realized by using a pneumatic actuator to actively adjust the tool compliance in the axial direction. Similar product can also be found in PushCorp Inc. However, the available active force controlled end effectors only have one degree of freedom (DOF). When grinding a part with complex curved surfaces, such as a blisk, the orientation of the end effector needs to be regulated all the time by the robot to make sure the actuating direction of the end effector matches the contact force direction. This process significantly slows down the moving speed of the robot and limits the efficiency of robotic grinding.

In this paper, a novel two DOFs contact force control algorithm is proposed for robotic blisk grinding with a smart end effector. The proposed method makes the end effector and the grinding tool adapt to the curvity change of the blisk surface and predict the amplitude and direction of the contact force in real time. The amplitude of the contact force is controlled by simultaneously manipulating the moving velocity of the grinding tool in both feed axes of the smart end effector. The tool path is generated and optimized so that the contact points are evenly distributed along the tool path on the workpiece surface. In the proposed methodology, the actuating directions of the end effector do not need to match the contact force direction all the time anymore, which significantly improves the efficiency of the robotic blisk grinding process by about six times.

2 Experimental setup

The proposed system configuration for robotic blisk grinding is shown in Fig. 1. A smart end effector is designed and installed on a Comau robot for active contact force control. A blisk is clamped to the work table through fixture 1 as the workpiece. The presented smart end effector is composed of a grinding tool, a spindle, a three-axis force sensor, a three-axis tilt sensor, and an XY positioning stage. The grinding tool is made by gluing a rubber cylinder to the tip of a steel rod and bonding a strip of abrasive paper outside the rubber cylinder. The spindle is fixed to the force sensor with fixture 2. The axial directions of both the spindle and the force sensor are arranged to be parallel with each other. The smart end effector senses the contact force between the grinding tool and the blisk with its integrated force sensor and a proposed force prediction algorithm. The relative angles between the global coordinate system and the force sensor axes are measured using the tilt sensor for gravity compensation. The force sensor and the tilt sensor are installed on the moving table of the XY stage through fixtures. The feed directions of the XY stage are parallel with the x and y axes of the force sensor. Two servo motors are connected to the ball-screws of the XY stage to drive it to move in its two feed directions. The information of the sensors, spindle and XY stage used in the smart end effector are given in Table 1.

During the robotic grinding process, the robot controls the primary position of the tool tip for blisk grinding, according to the optimized tool path. The smart end effector controls the amplitude of the contact force according to the force control algorithm. Please note that the experimental setup configuration presented in Fig. 1 can be used for both one DOF contact force control tests and two DOFs contact force control tests.

For one DOF contact force control tests, only one axis of the smart end effector (y-axis in Fig. 1 configuration) is controlled in the robotic grinding process. The feed direction of the smart end effector (y axis in Fig. 1) needs to be in the same direction as the normal direction of the workpiece surface at the working point (contact force direction) all the time during the grinding process. A one DOF controller is implemented to adjust the moving velocity of the feed axis (y axis in Fig. 1) of the XY stage to achieve the desired contact force.

For two DOFs contact force control tests, both axes of the smart end effector need to be controlled to realize the expected contact force control performance. The feed directions of the end effector do not need to match the contact force direction all the time anymore. The direction and amplitude of the contact force are identified with a force prediction algorithm. The velocities of both feed axes of the XY stage are manipulated according to the proposed two DOFs force control algorithm to achieve the expected contact force.

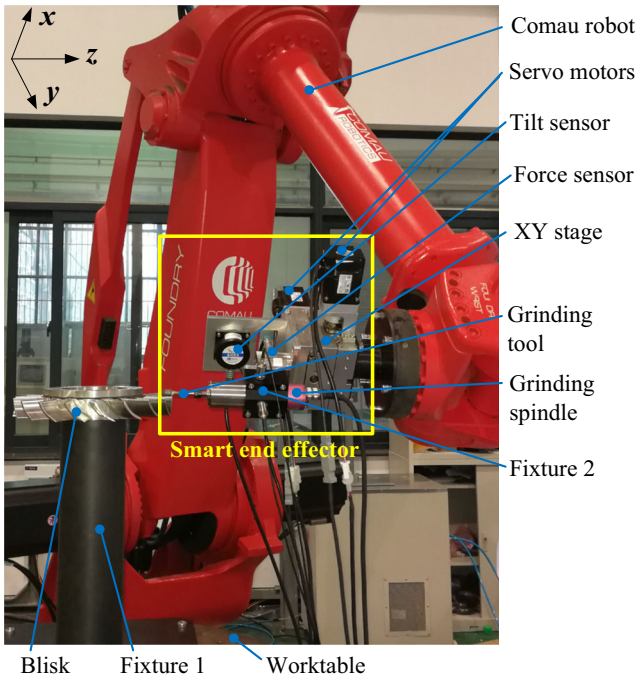

Fig. 1 Experimental setup configuration

3 System modeling and controller design

3.1 Configuration of the presented robotic grinding system

The block diagram of the presented two DOFs contact force controlled robotic grinding system is shown in Fig. 2. The tool path and the position commands of the robot are generated and optimized in advance for the robotic blisk grinding process. The robot controller receives the position commands and manipulates the robot gestures to achieve the expected tool path. The smart end effector controls the tool tip displacement in the contact force direction (a_p) during the robotic grinding process to achieve the expected contact force.

Figure 3 shows the forces loaded on the tooling system which is composed of the grinding tool, the grinding spindle, and the fixtures. The contact force (F_c) and the tangential grinding force (F_t) are loaded on the tip of the grinding tool. G is the gravity of the tooling system. $F_x^{'}$, $F_y^{'}$, and $F_z^{'}$ are the forces between the force sensor and the tooling system which are loaded on the clamping area of the fixture 3. The relevant forces sensed by the force sensor in the force sensor coordinates are F_x, F_y and F_z. ($F_x^{'}$, $F_y^{'}$, $F_z^{'}$) and (F_x, F_y, F_z) have the same amplitudes and opposite directions. Since the contact force (F_c) and the tangential grinding force (F_t) are parallel with the $F_x - F_y$ force plane, the forces in the F_z direction will not affect the amplitude F_c and F_t. Therefore, only the forces loaded in the x and y axes of the force sensor (F_x and F_y) are analyzed here. Assume the gravity components of the tooling system loaded in the x and y axes of the force sensor are G_x and G_y; the contact force components sensed in the x and y axes of the force sensor are F_{cx} and F_{cy}; the components of the tangential grinding force mapped in the x and y axes of the force sensor are F_{tx} and F_{ty}; the measured forces (F_x, F_y) can be obtained as

$$\begin{cases} F_x = F_{cx} + F_{tx} + G_x \\ F_y = F_{cy} + F_{ty} + G_y \end{cases} \tag{1}$$

The pitch, row and yaw angles (β_p, β_r, β_y) of the force sensor axes relative to the global coordinate system are measured with an embedded tilt sensor. The measured forces (F_x, F_y) and angles (β_p, β_r, β_y) are sent to the controller for prediction and control of the contract force (Fig. 2). The controller of the smart end effector includes a gravity compensation module, a force prediction module, and a force-position controller. The gravity compensation module calculates the gravity components loaded on the force sensor axes and removes them from the measured force signals (F_x, F_y). The output signals ($\overline{F}_x$, $\overline{F}_y$) of the gravity compensation module represent the measured forces that are resulted from the contact force (F_c) and the tangential grinding force (F_t) only, and they can be expressed as

$$\begin{cases} \overline{F}_x = F_x - G_x \\ \overline{F}_y = F_y - G_y \end{cases} \tag{2}$$

The force prediction module calculates the amplitude of F_c from the compensated force signals $\overline{F}_x$ and $\overline{F}_y$, and predicts the relative angle between the F_c direction and the positive F_x direction. The predicted amplitude ($\hat{F}_c$) and direction angle ($\hat{\alpha}$) of the contact force are passed to the force-position controller for active contact force control. The force-position controller is a multi-input-multi-output controller. Besides $\hat{F}_c$ and $\hat{\alpha}$, the other inputs include the expected contact force F_e, and the displacements (d_x, d_y) of the XY stage in its two feed directions. The controller outputs are the velocity commands (v_{xc}, v_{yc}) to the motor drivers that control the movements of the XY stage. Therefore, the tool tip displacement in the contact force axis (a_p) is adjusted to achieve the expected contact force. Also, the tool tip displacement in the tangential direction (a_t) resulted by the movements of the XY stage is controlled to be zero to avoid introducing extra positioning errors to the grinding process. The rotation speed of the grinding spindle is controlled by the spindle driver according to the velocity command v_{sc}.

3.2 Modeling of the tool tip displacements

The frequency response functions (FRFs) from the velocity command (in the voltage form) to the translational velocity of the smart end effector in its feed directions are measured, as

Table 1 Information of the devices used in the smart end effector

Items	Brand and model	Description
Force sensor	Liheng, LH-SZ-02	Three-axis force sensor; Range: 100 N in each axis
Tilt sensor	WitLink, VG400	Range: pitch ± 90°, roll ± 180°, heading 360°; Resolution: 0.1°
Spindle	Windward spindle, S4225-B40FL8	Maximum speed: 40000 RPM; Maximum torque: 13 N cm
XY stage	NSK, MC type two-axis table	Stroke: 50 mm × 50 mm; Pitch: 5 mm
Servo motors	YASKAWA, SGMJV-02ADE6S	Power: 200 W; Torque: 0.637 N m

shown in Figure 4. Sinusoidal signals at different frequencies are given as the inputs to the motor drives, and the resulted translational velocities (v_x, v_y) of both axes of the XY stage are recorded. From the measured FRFs, we can see that the dynamic relations from v_{xc} to v_x, and from v_{yc} to v_y can be both considered as a second order system. The related transfer functions are denoted as T_{vx} and T_{vy}, respectively, and their model parameters are identified as given in Table 2. Therefore, the tool tip velocities (v_x, v_y) and displacements (d_x, d_y) in the feed axes of the XY stage due to the motion control of the smart end effector can be expressed as

$$\begin{cases} v_i(s) = T_{vi}(s)v_{ic}(s) = \dfrac{b_i}{s^2 + 2\zeta_i\omega_{ni}s + {\omega_{ni}}^2}v_{ic}(s) \\ d_i = \dfrac{v_i(s)}{s} \end{cases}, \quad i = x, y \tag{3}$$

where b_i, ζ_i, and ω_{ni} are the model parameters of the transfer functions T_{vx} and T_{vy}.

The relations between the forces and displacements at the tool tip are explained in Fig. 5. The relative angle between the contact force (F_c) and the positive x-axis of the force sensor is denoted as α. The positive directions of the displacements (d_x, d_y) and the measured forces (F_x, F_y) are opposite to each other. It is the same case for the displacements (a_p, a_t) and the forces (F_c, F_t). The tool tip displacements in the contact force axis (a_p) and in the tangential direction (a_t) can be obtained by mapping the displacements d_x and d_y to their axes, and superposition the displacement components, as shown below:

$$\begin{bmatrix} a_p \\ a_t \end{bmatrix} = \underbrace{\begin{bmatrix} \cos\alpha & \sin\alpha \\ -\sin\alpha & \cos\alpha \end{bmatrix}}_{M_d} \begin{bmatrix} d_x \\ d_y \end{bmatrix} \tag{4}$$

where M_d is the transformation matrix from $[d_x, d_y]^{\mathrm{T}}$ to $[a_p, a_t]^{\mathrm{T}}$.

3.3 Modeling of the contact force and grinding force

The grinding tool is made by gluing a rubber cylinder to the tip of a steel rod and bonding a strip of abrasive paper outside the rubber cylinder. Since the flexibility of rubber is much larger than the steel rod and the amplitude of the contact force is small, only the deformation of the rubber part is considered in the modeling. When the tool tip just gets in contact with the workpiece, the contact force is zero, and the tool tip has a round shape without deformation. When the desired contact force is reached, the center of the tool tip has moved forward to the workpiece with a displacement a_c, and the rubber tip is deformed as shown in Fig. 6. The rubber tip is considered as a linear spring, and the contact force (F_c) can be modeled as

$$F_c = k_c a_c \tag{5}$$

where k_c is the spring coefficient of the rubber tip, which is about 3 N/mm. Assume the XY stage needs to move the tool tip towards the workpiece with a distance of a_0 in the negative F_c direction to make the tool tip and the workpiece just get in contact, the displacement a_c can be obtained as

$$a_c = a_p - a_0 \tag{6}$$

In order to explore the relation between the grinding force (F_t) and the contact force (F_c), Grinding tests are carried out with one DOF contact force control. The feed directions of the XY stage are arranged to be parallel with the directions of the contact force and the tangential grinding force respectively by path planning. Therefore, the values of the contact force and the grinding force can be directly measured with the force sensor after gravity compensation. Only the tool tip displacement in the feed direction that is parallel with the contact force direction is controlled in this test for contact force control. During the grinding tests, the contact force is controlled to stay at different values, and the amplitudes of both the contact force and the grinding force are recorded, as shown in Fig. 7. It can be found that the relation between the tangential

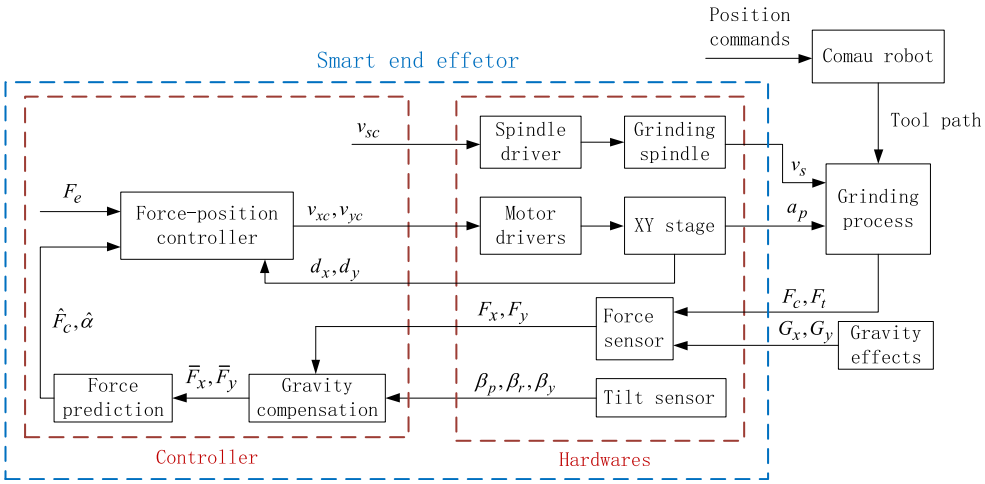

Fig. 2 Block diagram of the presented robotic grinding system

grinding force (F_t) and the contact force (F_c) can be approximated as

$$F_t = k_t F_c, \quad k_t \approx 0.3 \tag{7}$$

where k_t is a force coefficient.

3.4 Design of the gravity compensator

In order to accurately predict the contact force, the measured force signals (F_x, F_y) need to be gravity compensated. To compensate the gravity effects on the measured force signals, the gravity components (G_x, G_y) loaded on the force sensor axes need to be calculated and removed from the measured force signals. The gravity components can be obtained with the coordinates transformation method. Figure 8 shows the coordinate system relations of the smart end effector. The force sensor coordinate system (x-y-z) is assumed to be originally coinciding with the global coordinate system (P-Y-R). The rotational angles of the force sensor coordinate system (x-y-z) in the pitch, roll, and yaw directions are denoted as β_p, β_r, and β_y, respectively. These three rotational angles (β_p, β_r, β_y) are measured by the tilt sensor in the smart end effector. The transformation of the gravity (G) coordinates from the global coordinate system (P-Y-R) to the force sensor coordinate system (x-y-z) can be obtained as

$$\begin{bmatrix} G_x \\ G_y \\ G_z \end{bmatrix} = \underbrace{\begin{bmatrix} 1 & 0 & 0 \\ 0 & \cos\beta_p & \sin\beta_p \\ 0 & -\sin\beta_p & \cos\beta_p \end{bmatrix}}_{M_P} \underbrace{\begin{bmatrix} \cos\beta_r & \sin\beta_r & 0 \\ -\sin\beta_r & \cos\beta_r & 0 \\ 0 & 0 & 1 \end{bmatrix}}_{M_R} \underbrace{\begin{bmatrix} \cos\beta_y & 0 & -\sin\beta_y \\ 0 & 1 & 0 \\ \sin\beta_y & 0 & \cos\beta_y \end{bmatrix}}_{M_Y} \begin{bmatrix} 0 \\ G \\ 0 \end{bmatrix} = \begin{bmatrix} \sin\beta_r \\ \cos\beta_p\cos\beta_r \\ -\cos\beta_r\sin\beta_p \end{bmatrix} G \tag{8}$$

where $[G_x\ G_y\ G_z]^{\mathrm{T}}$ is the coordinate vector of the gravity (G) in the force sensor coordinate system (x-y-z). M_P, M_R, and M_Y are the coordinates transformation matrices for the pitch, roll, and yaw movements. Therefore, the gravity compensated forces can be obtained as

$$\begin{cases} \bar{F}_x = F_x - G_x = F_x - G\sin\beta_r \\ \bar{F}_y = F_y - G_y = F_y - G\cos\beta_p\cos\beta_r \end{cases} \tag{9}$$

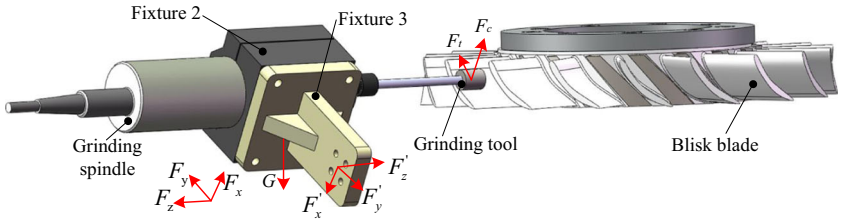

Fig. 3 Force analysis of the tooling system

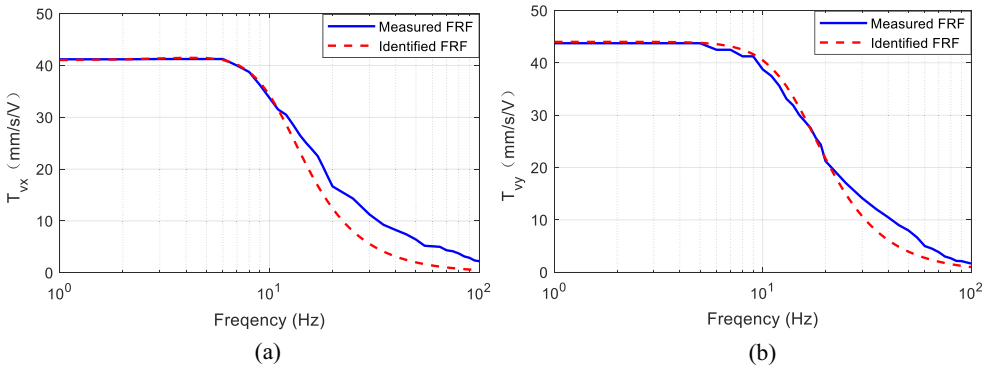

Fig. 4 The measured FRFs of the smart end effector, (a) FRF from v_{xc} to v_x; (b) FRF from v_{yc} to v_y

3.5 On-line prediction of the contact force

The amplitude and direction of the contact force (F_c) can be predicted from the compensated force signals ($\overline{F}_x, \overline{F}_y$). The relations between the forces (F_c, F_t) and ($\overline{F}_x$, $\overline{F}_y$) are shown in Fig. 9. $\overline{F}_x$ and $\overline{F}_y$ are the summation of the force components of F_c and F_t that are mapped on their axes, and can be expressed as

$$\begin{bmatrix} \overline{F}_x \\ \overline{F}_y \end{bmatrix} = \begin{bmatrix} \cos\alpha & -\sin\alpha \\ \sin\alpha & \cos\alpha \end{bmatrix} \begin{bmatrix} F_c \\ F_t \end{bmatrix} \tag{10}$$

The superposition of the forces F_c and F_t are the same as the superposition of the forces $\overline{F}_x$ and $\overline{F}_y$. Therefore, we have

$$|F_s| = \sqrt{\overline{F}_x{}^2 + \overline{F}_y{}^2} = \sqrt{F_c{}^2 + F_t{}^2} \tag{11}$$

where F_s is the resultant force of F_c and F_t. Substituting (7) into (11), we have

$$\sqrt{\overline{F}_x{}^2 + \overline{F}_y{}^2} = \sqrt{F_c{}^2 + (k_t F_c)^2} = F_c\sqrt{1 + k_t{}^2} \tag{12}$$

Thus, the predicted value ($\hat{F}_c$) of F_c can be calculated from $\overline{F}_x$ and $\overline{F}_y$ as

$$\hat{F}_c = \frac{\sqrt{\overline{F}_x{}^2 + \overline{F}_y{}^2}}{\sqrt{1 + k_t{}^2}} \tag{13}$$

Table 2 Model parameters of the system transfer functions

	b_i(mm · s/rad^2/V)	ζ_i(%)	ω_{ni}(rad/s)
T_{vx}	1.96×10^5	65	69.11
T_{vy}	3.91×10^5	70	94.25

The angle (γ) between F_c and F_s can be obtained as

$$\gamma = \text{atan}\left(\frac{F_t}{F_c}\right) = \text{atan}(k_t) \tag{14}$$

The angle ($\alpha + \gamma$) between $\overline{F}_x$ and F_s can be got as

$$\alpha + \gamma = \text{atan}\left(\frac{\overline{F}_y}{\overline{F}_x}\right) \tag{15}$$

Therefore, the predicted relative angle ($\hat{\alpha}$) between the contact force direction and the positive x-axis of the force sensor can be calculated as

$$\hat{\alpha} = \text{atan}\left(\frac{\overline{F}_y}{\overline{F}_x}\right) - \text{atan}(k_t) \tag{16}$$

3.6 Force-position controller design

The controller design goal is to control the contact force (F_c) to be the same as the expected value (F_e), and not to bring

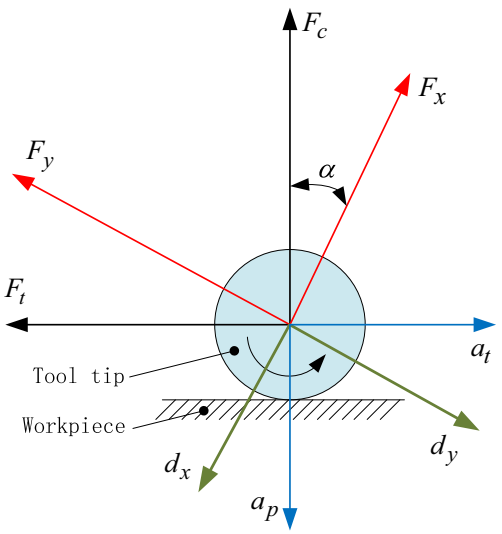

Fig. 5 Relations between the forces and displacements at the tool tip

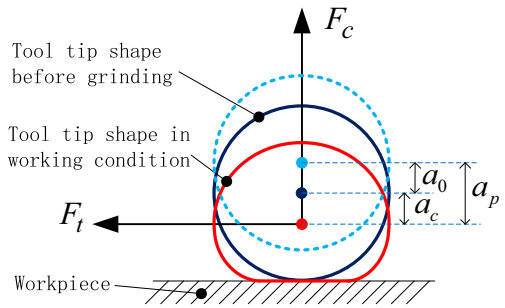

Fig. 6 Schematic diagram for the contact force modeling

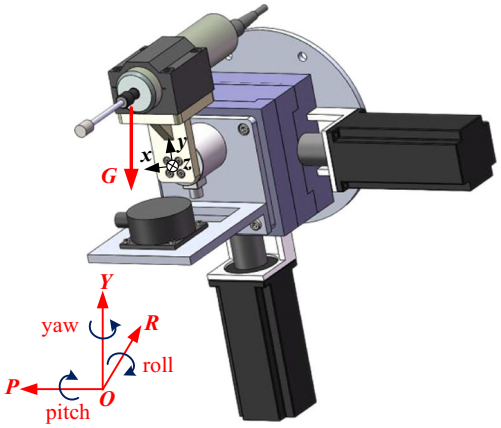

Fig. 8 Coordinate system relations of the smart end effector

extra positioning error to the grinding process ($a_t = 0$). The structure of the proposed force-position controller is shown in Fig. 10. It is composed of a force controller, a position controller, and a transformation matrix. PI control structure is implemented in the design of both the force controller and the position controller, as shown below:

$$v_p(s) = \left(k_{p1} + \frac{k_{i1}}{s}\right)\left(F_e(s) - \hat{F}_c(s)\right) \tag{17}$$

$$\begin{cases} v_t(s) = \left(k_{p2} + \frac{k_{i2}}{s}\right)(0 - a_t(s)) \\ a_t(s) = -d_x(s)\sin\hat{\alpha} + d_y(s)\cos\hat{\alpha} \end{cases} \tag{18}$$

where v_p and v_t are the outputs of the force controller and position controller, respectively. The tool tip displacement in the tangential direction (a_t) resulted by the movements of the XY stage is calculated from the tool tip displacements (d_x, d_y). k_{pj}, k_{ij} ($j = 1,2$) are the proportional gains and integral gains of the controllers, respectively. The proportional gains (k_{p1}, k_{p2}) are tuned to adjust the responding speed of the force control loop and position control loop. Larger proportional gains give a faster responding speed. The integral gains (k_{i1}, k_{i2}) are tuned to adjust the steady state error of the controlled force (F_c) and tool tip position (a_t). A larger integral gain leads to a lower steady-state error. However, if the gains are too large, the system may become unstable. Therefore, both the proportional and integral

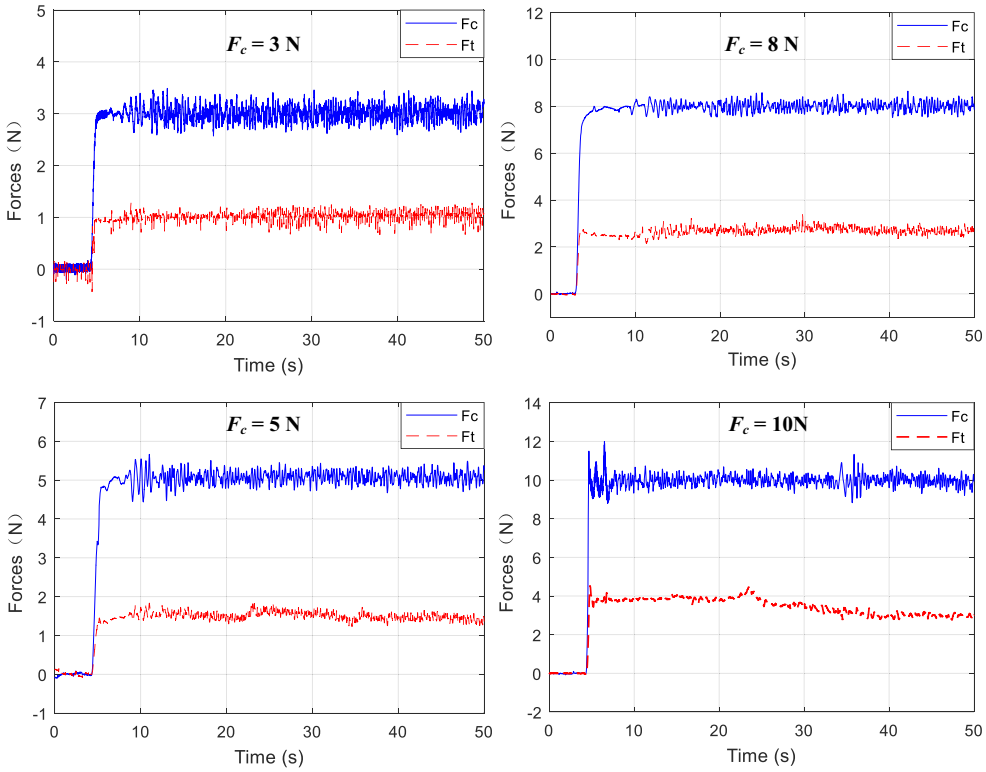

Fig. 7 Measured contact forces (F_c) and tangential grinding forces (F_t)

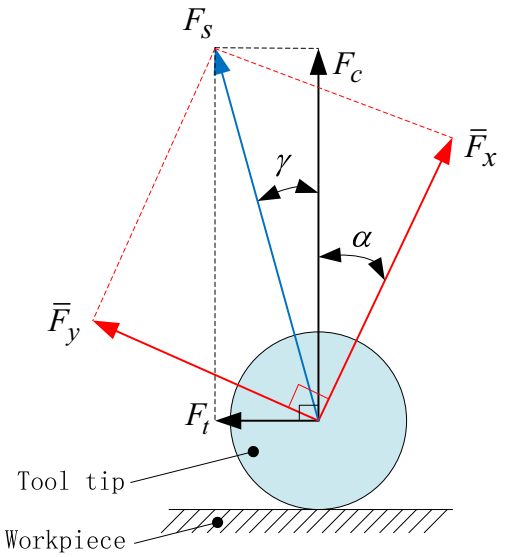

Fig. 9 Relation between the contact force (F_c), grinding force (F_t), and the compensated forces ($\bar{F}_x$, $\bar{F}_y$)

gains need to be carefully tuned to achieve a satisfying control performance.

The physical meanings of v_p and v_t are the velocity commands of the tool tip in the a_p and a_t directions (Fig. 5). In order to get the expected velocities (v_{xc}, v_{yc}) of the XY stage in their feed directions (d_x and d_y directions in Fig. 5), the inverse matrix of M_d which is defined in (4) is implemented as a transformation matrix for the controller outputs (v_p, v_t). Therefore, the desired velocity commands can be obtained as:

$$\begin{bmatrix} v_{xc} \\ v_{yc} \end{bmatrix} = \underbrace{\begin{bmatrix} \cos\alpha & -\sin\alpha \\ \sin\alpha & \cos\alpha \end{bmatrix}}_{M_d^{-1}} \begin{bmatrix} v_p \\ v_t \end{bmatrix} \tag{19}$$

4 Tool path generation and optimization

4.1 Tool path generation for robotic blisk grinding with one DOF force control

The tool path for the robotic blisk grinding process is planned in advance with the commercial software MasterCAM, and the position commands of the robot are generated using Robotmaster CAD/CAM. In robotic grinding with one DOF force control, the feed direction of the smart end effector needs to be in the same direction as the normal direction of the workpiece surface at the working point (contact force direction) when generating the tool path. The generated tool path for robotic grinding of a blisk blade with one DOF force control is shown in Fig. 11. The tool points are dense in the areas where the curvity is large, while the tool points are sparse at the locations where the curvity is small. The time that a robot spends to move between each two adjacent points is the same. Therefore, around the leading and training edges where the tool points are dense, the grinding tool moves very slowly, and this may cause excessive grinding of the blade. In some areas of the convex and concave surface where the tool points are sparse, the grinding tool moves very fast, and this may cause insufficient grinding of the blade.

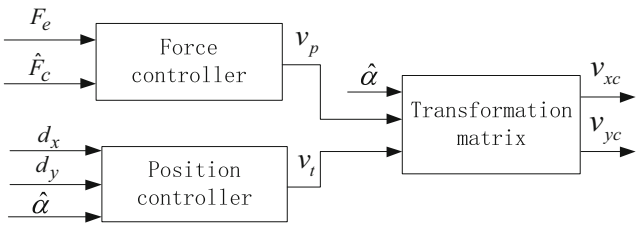

Fig. 10 Structure of the proposed force-position controller

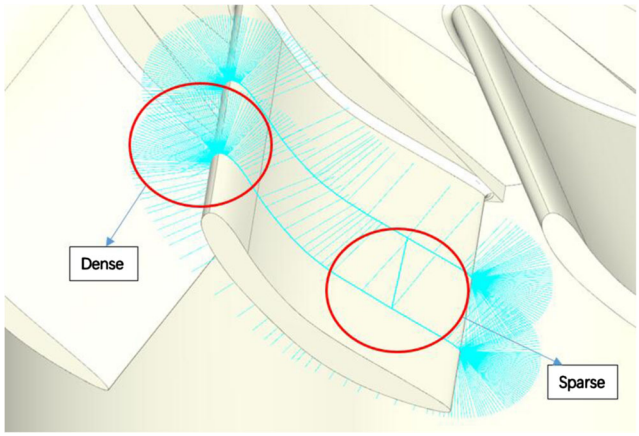

Fig. 11 Tool path for robotic grinding with one DOF force control

4.2 Tool path generation for robotic blisk grinding with two DOFs force control

In robotic grinding with our proposed two DOFs force control method, the grinding tool can be controlled to automatically adapt to the curvity change of the blisk blade, and maintain a

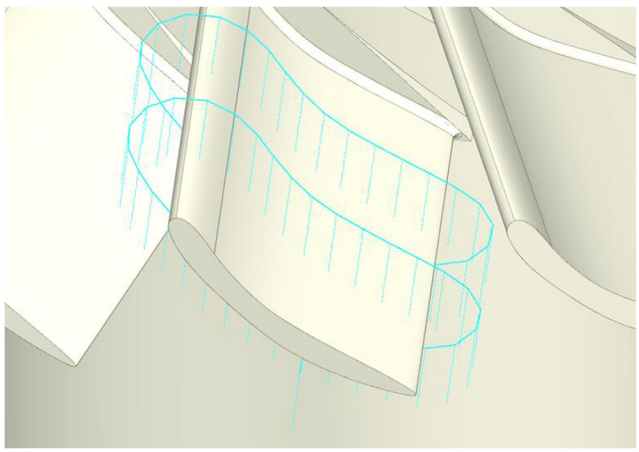

Fig. 12 Tool path for robotic grinding with two DOFs force control

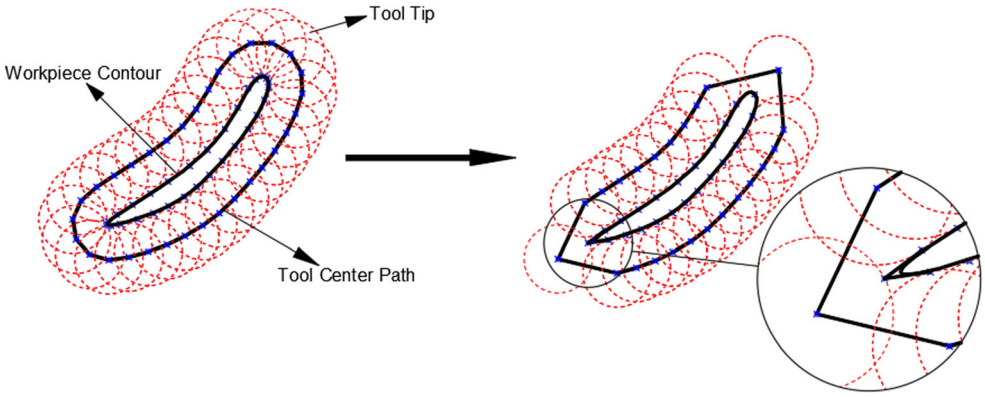

Fig. 13 Optimization of the tool path

constant contact force as expected. The relative angle between the contact force direction and the feed axis of the smart end effector can be predicted with the presented force prediction algorithm. Also, the amplitude of the contact force can be well controlled by manipulating the moving velocities of both feed axes of the smart end effector according to the control commands. In this way, the control force direction can automatically match the desired contact force direction. Therefore, one of the feed directions of the smart end effector does not need to be collinear with the contact force direction all the time anymore. Due to this effect, the tool path can be generated with the tool tip points evenly distributed, as shown in Fig. 12. Thus, a constant feed rate of the robotic grinding process can be achieved, which can solve the excessive and insufficient grinding problems in some extent.

4.3 Tool path optimization

For the tool path shown in Fig. 12, the tool tip points are uniformly distributed. However, these points represent the tool center points. The contact points between the tool tip and the workpiece contour are still not distributed evenly, as shown in the left part of Fig. 13. The contact points are dense near the leading and trailing edges, and are uniform around the concave

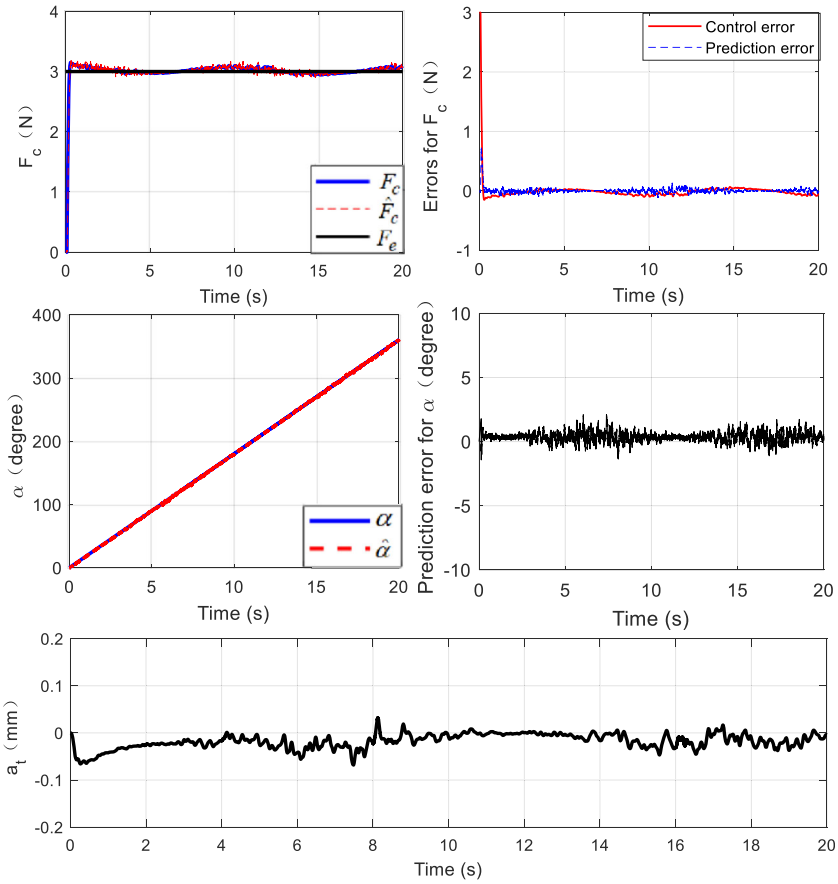

Fig. 14 Simulated contact force (F_c), direction angle (α) and tangential tool tip displacement (a_t), when the expected contact force (F_e) is set to 3 N

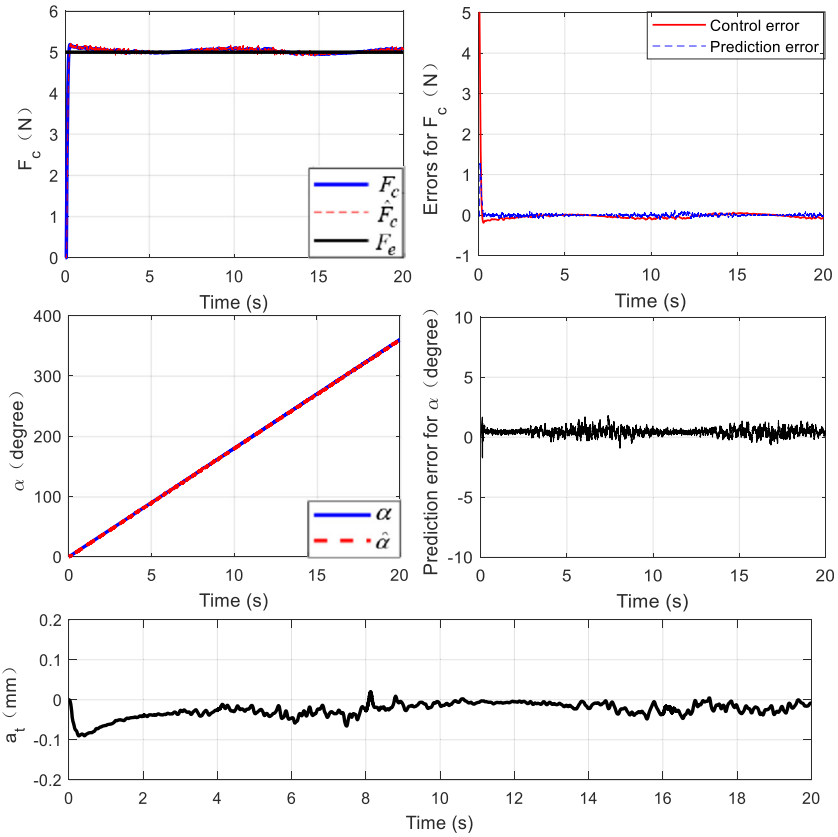

Fig. 15 Simulated contact force (F_c), direction angle (α) and tangential tool tip displacement (a_t), when the expected contact force (F_e) is set to 5 N

and convex surfaces. In order to make the dense contact points around the leading and trailing edges distributed more evenly, we first calculated the trajectory of the contact points from the tool center path. Then, we calculated the distance between each two adjacent contact points along the trajectory. For the contact points around the leading and trailing edges, we manually delete the contact points whose distance in between are much smaller than the regular distance between two adjacent contact points in the concave and convex areas and make the contact points distribute evenly, as shown in the right part of Fig. 13. The tool center points which relate to the remaining contact points are used as the tool path for robotic grinding. In this way, the contact points on the workpiece contour are uniformly distributed, which can further improve the performance of the robotic blisk grinding process.

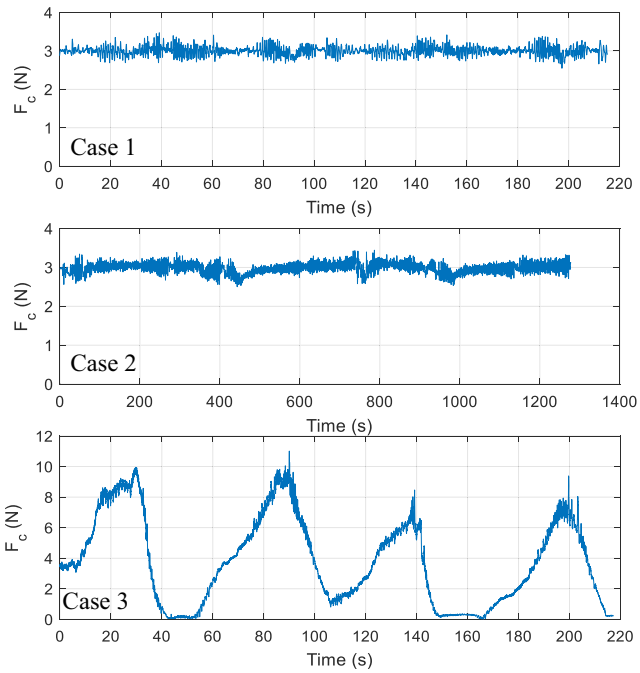

Fig. 16 The measured contact forces in different cases during the robotic blisk grinding tests

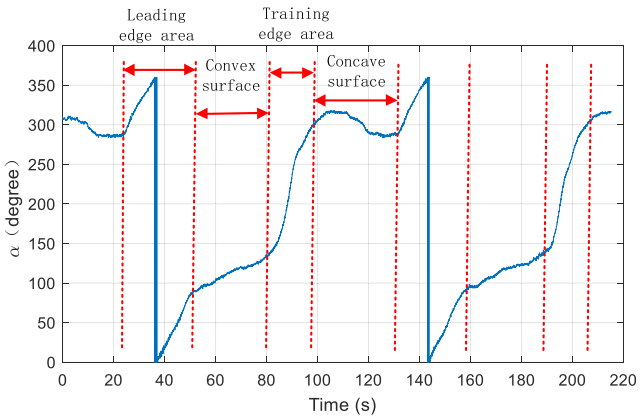

Fig. 17 The measured trajectory of the contact force angle (α)

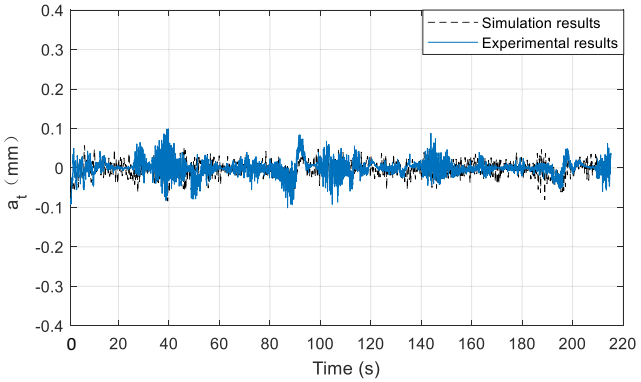

Fig. 18 The measured and simulated tool tip displacement (a_t) in the tangential direction

5 Simulation analysis

The performance of the prediction and control of the contact force, as well as the tool tip displacement control in the tangential direction, is validated by simulation in this section. The system model used in the simulation is built according to the system structure shown in Fig. 2. Since the spindle speed does not contribute much to the contact force and the grinding force in our grinding tests, the spindle driver and grinding spindle modules (Fig. 2) are ignored in the simulation model. The direction angle (α) of the contact force will change continuously during the robotic blisk grinding process. Therefore, a ramp signal from 0° to 360° is used to simulate the change of α when calculating the tool tip displacements (a_p, a_t) from the displacements (d_x, d_y) of the XY stage. In the simulation, the initial distance between the tool tip and the workpiece (a_0) is assumed to be 0.5 mm. The positioning error of the Comau robot is considered as a sinusoidal disturbance with 0.3 mm amplitude and 0.1 Hz frequency. This disturbance is directly added to the tool tip displacement a_p. White noise signals are added to the simulated force sensor outputs (F_x, F_y) to estimate the real work conditions. The expected contact force (F_e) is set to 3 N and 5 N respectively to test the control and prediction performance.

In the simulation, the controller parameters are tuned to $k_{p1} = 0.08$, $k_{i1} = 0.009$, $k_{p2} = 0.2$, $k_{i2} = 0.1$, according to the tuning method explained in section 3.6. The simulated results are given in Figs. 14 and 15. The control error for F_c represents the difference between the expected contact force and the real contact force ($F_e - F_c$), and the prediction error for F_c indicates the difference between the real contact force and the predicted contact force ($F_c - \hat{F}_c$). The prediction error for α represents the difference between the real direction angle and the predicted direction angle ($\alpha - \hat{\alpha}$). It can be found that the contact force (F_c) is well controlled to the expected values (F_e) in both cases with less than 0.2 N control errors, and the predicted contact force ($\hat{F}_c$) matches the real contact force (F_c) in the grinding process with less than 0.1 N prediction error. The large control error happening when the simulation time is close to zero is due to the fact that the real contact force (F_c) needs a response period to rise from zero to the expected value (F_e). The direction angle (α) of the contact force is also predicted. The maximum prediction errors are less than 2°. The prediction error is mainly caused by the noise added in the force sensor output signals. The tool tip displacement in the tangential direction (a_t) is controlled to be zero in the simulation. It can be seen that the maximum amplitudes of a_t are about 0.065 mm and 0.090 mm for the cases in Fig.14 and Fig. 15, respectively. Therefore, it adds almost no additional positioning error to the original grinding process.

6 Experimental results

In order to further validate the effectiveness of the proposed contact force control method, robotic blisk grinding experiments are carried out in three different cases: (1) with our proposed two DOFs force control method; (2) with one DOF force control method; (3) without force control. The orientation of the smart end effector is different in case 2 compared to that in cases 1 and 3. In case 2, the one DOF force control method requires the feed direction of the smart end effector to be the same as the contact force direction. Therefore, the robot needs to adjust the orientation of the smart end effector all the time during the grinding process.

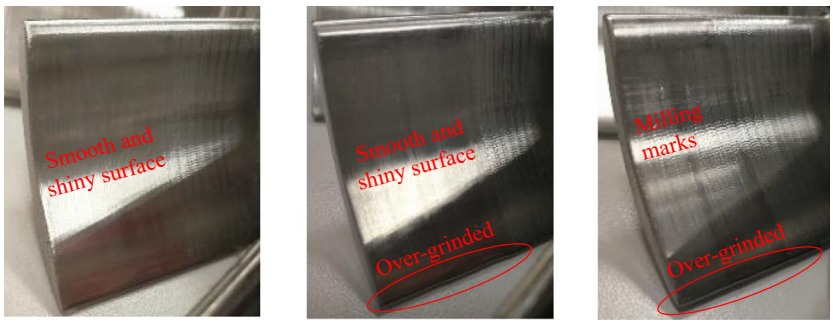

Case 1: with 2 DOFs force control | Case 2: with 1 DOF force control | Case 3: without force control

Fig. 19 The surface finish of the grinded blisk blades in different cases

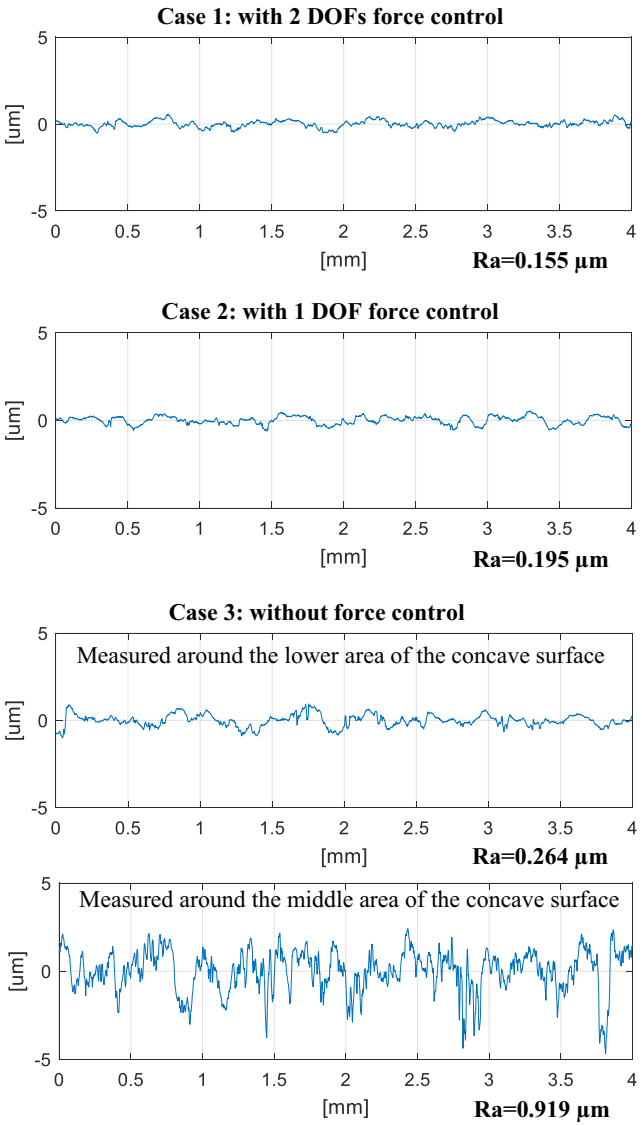

Fig. 20 The measured surface roughness of the grinded blisk blades in different cases

But in cases 1 and 3, the orientation of the smart end effector needs to be seldom adjusted. In the robotic grinding experiments, the controller parameters (k_{p1}, k_{i1}, k_{p2}, k_{i2}) in case 1 are the same as the ones used in the simulation in section 5. In case 2, a PI controller with a proportional gain of 0.08, and an integral gain of 0.009 is implemented for one DOF contact force control. The measured contact forces in these three different cases are shown in Fig. 16.

In cases 1 and 2, the expected contact force is set to 3 N. It can be found that the contact force is well controlled to the expected value, and the force fluctuation is less than 1 N in both cases. When the blisk blade is grinded without force control (case 3), the contact force fluctuation is much larger than that in the cases with force control. Comparing the machining time cost in cases 1 and 2, we can see that the machining time in case 1 is about 215 s, while it is around 1277 s in case 2, which is about 6 times longer. This is due to the reason that the robot needs to always adjust the orientation of the smart end effector in case 2 to make sure its feed direction is the same as the normal direction of the blisk blade at each working point. This greatly slows down the grinding process, especially when grinding the leading and training edges, where the curvity change is severe. Moreover, grinding the leading and training edges for too long a time may lead to over-grinding of the edges, and may damage the blisk.

In case 1, the measured trajectory of the contact force angle (α) and the tool tip displacement (a_t) in the tangential direction are shown in Figs. 17 and 18, respectively. Since the range of α is set to [0360°], the value of α starts from 0° again when it reaches 360°. It can be found that the contact force angle (α) changes dramatically around the leading and training edges, and changes gradually along the concave and convex surfaces. The tool tip displacement in the tangential direction (a_t) is controlled to be zero. The experimental results of a_t are compared with the simulation results which uses the values of the measured contact force angle (α) in the simulation. It can be seen that the experimental results and the simulation results match each other, and the maximum controlling error of a_t is less than 0.1 mm. Therefore, the proposed two DOFs force control method adds almost no additional positioning error to the original robotic grinding process.

The surface finish of the grinded blisk blades in different cases are shown in Fig. 19. With force control (cases 1 and 2), the grinded blade surface is smooth and shiny, and the milling marks are well removed. Without force control (case 3), the milling marks in the middle area of the concave surface can still be clearly seen. But they are removed in the areas that are close to the leading and training edges. This is because the contact force in case 3 is large around the leading and training edge areas, and it is small in the concave and convex surfaces, as shown in Fig. 16 (case 3). From Fig. 19, it can also be found that the training edges of the blisk blades in cases 2 and 3 are over-grinded. This is due to that the tool path points for case 2 is too dense around the training edge area, causing that area been grinded for too long a time, while the contact force is too large around the training edge area in case 3, leading to excessive grinding of that area. In case 1, with the proposed two DOFs force control, the blisk blade is not over-grinded, and the surface quality is good.

The measured average surface roughness (Ra) of the blisk blades in different cases are shown in Fig. 20. With force control (cases 1 and 2), the surface quality is uniformly good. The measured Ra is 0.155 µm for case 1, while it is 0.195 µm for case 2. Without force control (case 3), since the contact force fluctuates significantly along the tool path, the surface quality is not uniform in different areas of the blade surface. The middle area of the concave surface, where the contact

force is very small, is not grinded sufficiently, resulted in a large Ra of 0.919 μm. The milling marks in the lower area of the concave surface are well removed, since the contact force is large, therefore, leading to a small Ra of 0.264 μm.

7 Conclusion

In this paper, a novel two DOFs contact force control method is proposed for robotic blisk grinding process. A smart end effector is developed and used as the actuating device for contact force control. The direction and amplitude of the contact force is measured with a force prediction algorithm, and the contact force is controlled with a force-position controller. The tool path is generated and optimized so that the contact points between the tool tip and workpiece are evenly distributed along the grinding path. Both simulation and experiments are carried out to evaluate the performance of the proposed method. The following conclusions are obtained.

(1) The proposed contact force prediction algorithm can well predict the direction and amplitude of the contact force. The predicted direction angle ($\hat{\alpha}$) matches the real value (α) with less than 2° error. The error is mainly caused by the noise in the force sensor signals. The predicted contact force agrees with the real contact force very well, and the prediction error is less than 0.1 N.
(2) The contact force is well controlled to the expected value with the proposed two DOFs force control method. The force fluctuation is less than 1 N. Without force control, the force fluctuation can reach about 10 N.
(3) The tool tip displacement in the tangential direction (a_t) resulted by the movements of the smart end effector is controlled to be zero. The maximum control error is less than 0.1 mm in both simulation and experiments. Therefore, the proposed two DOFs force control method introduces almost no extra positioning errors to the original grinding process.
(4) With the proposed two DOFs contact force control method, the grinding tool is controlled to automatically adapt to the curvity change of the blisk blade, and maintain a constant contact force as expected. Therefore, the robot does not need to adjust the orientation of the end effector to match the contact force direction any more. Also, the tool path can be generated to be more evenly distributed to improve the efficiency and surface quality. Experimental results show that the efficiency of the robotic blisk grinding process improves by about six times, compared to the case with one DOF force control.
(5) Great surface finish quality of the blisk blade is achieved with the proposed two DOFs contact force control method, and the average surface roughness is 0.155 μm. With one DOF force control, although the surface finish is also good with a Ra of 0.195 μm, the training edge is over-grinded. Without force control, the surface finish is poor. Because the contact force varies significantly along the tool path, some areas are insufficient grinded (milling marks are not well removed), and some other areas (e.g., the training edge) are over-grinded.

Acknowledgements This research is supported by the National Natural Science Foundation of China (Grant Nos. 51705175, 91748114 and 51535004) and the China Postdoctoral Science Foundation (Grant No. 2017M612444).

Publisher's Note Springer Nature remains neutral with regard to jurisdictional claims in published maps and institutional affiliations.

References

1. Xu X, Zhu D, Zhang H, Yan S, Ding H (2017) TCP-based calibration in robot-assisted belt grinding of aero-engine blades using scanner measurements. Int J Adv Manuf Technol 90:635–647. https://doi.org/10.1007/s00170-016-9331-8
2. Liang W, Kang X, Zhao W, Yang Y (2016) Electrical discharge machining of electron beam melting formed shrouded blisk. Int J Adv Manuf Technol 87:2319–2326. https://doi.org/10.1007/s00170-016-8545-0
3. Ren JX, Yao CF, Zhang DH, Xue YL, Liang YS (2009) Research on tool path planning method of four-axis high-efficiency slot plunge milling for open blisk. Int J Adv Manuf Technol 45:101–109. https://doi.org/10.1007/s00170-009-2153-1
4. Zhang J, Shi Y, Lin X, Li Z (2017) Parameter optimization of five-axis polishing using abrasive belt flap wheel for blisk blade. J Mech Sci Technol 31:4805–4812. https://doi.org/10.1007/s00170-017-0717-z
5. Huang H, Gong ZM, Chen XQ, Zhou L (2002) Robotic grinding and polishing for turbine-vane overhaul. J Mater Process Technol 127:140–145. https://doi.org/10.1016/S0924-0136(02)00114-0
6. Duan J, Zhang Y, Shi Y (2016) Belt grinding process with force control system for blade of aero-engine. Proc Inst Mech Eng Part B J Eng Manuf 230:858–869. https://doi.org/10.1177/0954405414563420
7. Zhao P, Shi Y (2014) Posture adaptive control of the flexible grinding head for blisk manufacturing. Int J Adv Manuf Technol 70:1989–2001. https://doi.org/10.1007/s00170-013-5438-3
8. Xiao G, Huang Y (2015) Constant-load adaptive belt polishing of the weak-rigidity blisk blade. Int J Adv Manuf Technol 78:1473–1484. https://doi.org/10.1007/s00170-014-6724-4
9. Xiao G, Huang Y (2016) Equivalent self-adaptive belt grinding for the real-R edge of an aero-engine precision-forged blade. Int J Adv Manuf Technol 83:1697–1706. https://doi.org/10.1007/s00170-015-7680-3
10. Xiao G, Huang Y, Yin J (2017) An integrated polishing method for compressor blade surfaces. Int J Adv Manuf Technol 88:1723–1733. https://doi.org/10.1007/s00170-016-8891-y
11. Roswell A, Xi F, Liu G (2006) Modelling and analysis of contact stress for automated polishing. Int J Mach Tools Manuf 46:424–435. https://doi.org/10.1016/j.ijmachtools.2005.05.006
12. Thomessen T, Lien TK, Sannñs PK (2001) Robot control system for grinding of large hydro power turbines. Ind Robot An Int J 28:328–334
13. Dai H, Yuen KM, Elbestawi MA (1993) Parametric modelling and control of the robotic grinding process. Int J Adv Manuf Technol 8:182–192

14. Minami M, Asakura T, Dong LX, Huang YM (1996) Position control and explicit force control of constrained motions of a manipulator for accurate grinding tasks. Adv Robot 11:285–300. https://doi.org/10.1163/156855397X00254
15. Sun Y, Giblin DJ, Kazerounian K (2009) Accurate robotic belt grinding of workpieces with complex geometries using relative calibration techniques. Robot Comput Integr Manuf 25:204–210. https://doi.org/10.1016/j.rcim.2007.11.005
16. Pan Z, Zhang H (2008) Robotic machining from programming to process control:a complete solution by force control. Ind Robot An Int J 35:400–409. https://doi.org/10.1109/WCICA.2008.4594434
17. Zhang J, Liu G, Zang X (2016) A hybrid passive / active force control scheme for robotic belt grinding system. In: Proceedings of 2016 IEEE international conference on mechatronics and automation, August 7–10,Harbin, China
18. Chen SY, Zhang T, Zou YB (2017) Fuzzy-sliding mode force control research on robotic machining. J Robot 2017:1–8. https://doi.org/10.1155/2017/8128479
19. Liao L, Xi F, Liu K (2008) Modeling and control of automated polishing/deburring process using a dual-purpose compliant toolhead. Int J Mach Tools Manuf 48:1454–1463. https://doi.org/10.1016/j.ijmachtools.2008.04.009